

Theory and shape optimization of acoustic driven triboelectric nanogenerators

Z. Zhang ^{a,b,1}, J. Shao ^{a,b,1}, Y. Nan ^{a,b}, M. Willatzen ^{a,b,***}, Z.L. Wang ^{a,b,c,*}

^a Beijing Institute of Nanoenergy and Nanosystems, Chinese Academy of Sciences, Beijing, 101400, PR China

^b School of Nanoscience and Technology, University of Chinese Academy of Sciences, Beijing, 100049, PR China

^c School of Materials Science and Engineering, Georgia Institute of Technology, Atlanta, GA, 30332-0245, United States



ARTICLE INFO

Keywords:

Triboelectric nanogenerator
Acoustic transducer
Electro-mechano-acoustical circuits analogy
Finite element method
Multi-physical field coupling

ABSTRACT

As a clean, sustainable, and widely distributing energy source, acoustic waves are rarely available for energy conversion because of their high entropy and low energy density. Although the triboelectric nanogenerator (TENG) has been utilized for efficient acoustic energy harvesting, and most works are focusing on the design and geometry structures of TENG devices towards specific applications, a theoretical framework and models of the complex energy conversion system are still limited. Here, a multi-physical field coupling model of an acoustic driven TENG is presented that establishes the theoretical guidelines and optimal strategies for a typical acoustic energy system. This coupling model is composed of a basic acoustic transducer model, a TENG model, and an external circuit model coupling the acoustic field, mechanical field, and the quasi-electrostatic field. Using the finite element method (FEM), the energy conversion process including acoustic vibrations, wave propagation, and transducer reception are simulated systematically which allow us to reveal the dynamic power output behaviors of the acoustic driven TENG. The built multi-physical model and comprehensive analysis in this work provides a new research frame and platform for the design, optimization, and application of the TENG acoustic energy harvesting system.

1. Introduction

With the rapid development of artificial intelligence (AI) and the Internet of things (IoTs), the power demands have increased vastly but the corresponding supply has not [1–6]. As a clean, sustainable, and widespread energy source, acoustic waves are omnipresent in our surroundings, from mechanical vibration to human activity, soothing music to traffic noise which could serve as an ideal power supply for sensors [7, 8]. Unfortunately, acoustic energy has not been widely utilized due to its low energy density and the lack of effective technologies for energy conversion [9,10]. Triboelectric nanogenerators (TENGs), based on Maxwell's displacement current as the driving force to convert distributed and disorganized mechanical energy into electricity [11–15], have shown great potential in both energy harvesting [16–21] and self-powered systems [19,20,22–24]. In addition, the small-size, low-cost, light-weight, and especially high efficiency character of TENGs at a low frequency makes them a possible candidate for harvesting acoustic

wave energy to drive multifunctional sensors for AI and IoTs [8,25,26].

A typical acoustic driven TENG consists of at least two different triboelectric layers functioning as the diaphragm and substrate, respectively, and two electrodes connected to the external circuit [27]. When the diaphragm is in contact with the substrate, tribo-charges are generated at the contacting surfaces whereby a displacement current is established [28,29]. Until now, numerous TENG devices have been designed and fabricated with various tribo-materials or geometric configurations [27,30–32] so as to increase the output power and acoustic energy conversion efficiency as required by a self-powered system [33]. However, previously published reports have focused on the structural optimization and power output of the TENG device [34–38] while paying less attention to the corresponding theoretical model and dynamic analysis of the acoustic energy harvesting system, largely because the latter involves several disciplines of expertise.

To establish a suitable model, there are three key points to consider. Firstly, the effect of the sound field on TENG output requires attention.

* Corresponding author.

** Corresponding author.

E-mail addresses: mortenwillatzen@binn.cas.cn (M. Willatzen), zlwang@binn.cas.cn (Z.L. Wang).

¹ These authors contributed equally to this work.

Secondly, the frequency of the acoustic pressure waves as well as the physical boundaries of the sound field play important roles. Last, but not least, an effective method is needed to simulate the acoustic energy harvesting process consisting of three subsystems in the form of acoustics, mechanics, and electricity modules. To solve this problem, the finite element method (FEM) software COMSOL has been adopted, to effectively display the dynamic simulation process of energy conversion.

In this work, we propose a multi-physical field coupling model to clarify how the acoustic energy is converted into electricity through an acoustic driven TENG energy harvesting system. Firstly, the basic vibration modes of the diaphragm and the relationship between the

deformation and output potential are modeled and simulated. Then, we investigate the effects of the pressure load, vibration frequency, different wave types (plane waves and spherical waves), and acoustic field conditions (with or without matching layer) on the basic outputs of the energy acoustic energy conversion system. It is known that the maximum output of the acoustic driven TENG is obtained at the resonance frequency. Specifically, a better response occurs at the low-frequency band of the plane wave acoustic field, and the anechoic environment simulated by the acoustic matching layer can also improve the performance of the TENG acoustic transducer. In addition, from a comprehensive consideration of the combined influence of geometric

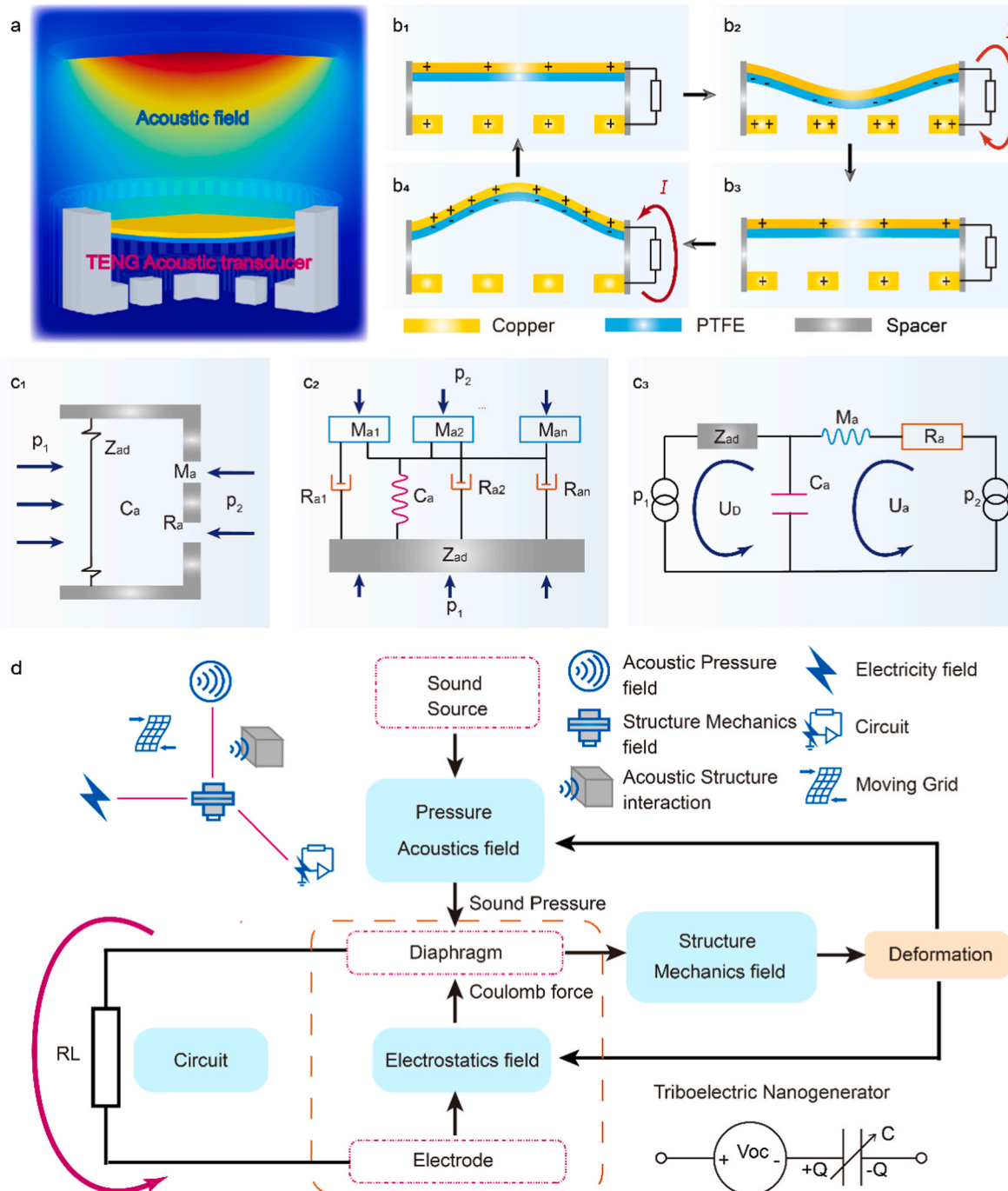


Fig. 1. Structure of acoustic driven triboelectric nanogenerator (TENG), electro-mechano-acoustical circuits analogy, and the whole simulation workflow (a) Structure of TENG acoustic transducer in acoustic field. (b) Working principle of TENG acoustic transducer (in one cycle). (c) Schematic illustrations of acoustic structure (c₁), mechanics analogy (c₂), and electricity analogy (c₃) of TENG acoustic transducer (d) Simulation process and physical field used in the finite element analysis method.

structures and circuit conditions, general strategies of the TENG acoustic transducer can be developed to optimize the acoustic energy harvesting process.

2. Result and discussion

2.1. Basic structure and working mechanism

The acoustic driven TENG in this simulation has a sandwich structure composed of three vertical layers [27]. It consists of a thin film of dielectric polytetrafluoroethylene (PTFE) with permanent negative charges stored on the surface as the diaphragm and two copper layers (Parameters utilized in the numerical calculations can be found in Note S1). One layer of copper is used as the substrate and electrode while the other one is laminated on the PTFE diaphragm as the electrode (Fig. 1a). Holes are introduced in the bottom layer of copper in order to reduce the air friction which to dampen the vibrations. When acoustic waves are incident on the TENG acoustic transducer, vibration in its composite diaphragm composed of PTFE and Cu is established, which leads to the contact and separation of the diaphragm and substrate copper layer. Contact electrification generates charges on both diaphragm and substrate surfaces (Fig. 1b₁). PTFE, owing to a greater electronegativity, will gain electrons from copper whereby it becomes negatively charged, while the substrate copper layer becomes positively charged. Due to the acoustic pressure difference, the diaphragm and substrate will be separated and a potential difference between the two electrodes is established which is the driving force to generate current flowing through the external circuit. As a result, free electrons are driven from the upper electrode to the substrate copper electrode to maintain balance in the local electric field. The redistribution of charge also makes the substrate copper electrode more positively charged than the upper copper layer on PTFE. This flow of electrons will continue until the separation between the two films reaches a maximum (Fig. 1b₂). The next excitation makes the diaphragm move towards the substrate resulting in a reversed current flow from the substrate electrode to the upper electrode (Fig. 1b₃). Finally, the surfaces of PTFE and the copper substrate come into contact again, with the electrical charge distribution returning to its initial state, completing a full cycle of electricity generation (Fig. 1b₄). With continuous incident acoustic wave energy, contact, and separation occurring alternately, another cycle of electricity generation begins.

2.2. Electro-mechano-acoustical circuits analogy

A simple schematic illustration of the TENG acoustic transducer is shown in Fig. 1c₁. The diaphragm serves as the mass suspended on a spring. The loss of a mechanical system is defined as a resistance. When the incident acoustic wavelength is much larger than the geometrical dimensions of the transducer, the internal structure of the TENG acoustic transducer can be seen as a Helmholtz resonant cavity. The equivalent impedance of the diaphragm and cavity structure are Z_{ad} and Z_a respectively, defined by Refs. [39,40]:

$$Z_{ad} = R_{ad} + j\omega M_{ad} + \frac{1}{j\omega C_{ad}} \quad (1)$$

$$Z_a = R_a + j\omega M_a + \frac{1}{j\omega C_a} \quad (2)$$

where R_{ad} , M_{ad} and C_{ad} represent equivalent acoustic resistance, mass, and compliance, respectively. R_a , M_a and C_a describe the acoustic resistance, mass, and compliance caused by holes and cavities.

As shown in Fig. 1c₂, the Helmholtz resonator can also be modeled as a mass-spring-damper system. The air in the holes vibrates as a mass and the air inside the cavity acts as a spring. Besides, considering the transmission losses due to the friction, a damper must be added to the mechanical analogy system (a more specific explanation can be found in

Note S2). Furthermore, in order to simplify this system, an electricity analogy is proposed in Fig. 1c₃. According to Kirchhoff's law, two equations governing the acoustic pressure are obtained [39]:

$$U_D \left(Z_{ad} + \frac{1}{j\omega C_a} \right) - \frac{U_a}{j\omega C_a} = p_1 e^{j\omega t} \quad (3)$$

$$-\frac{U_D}{j\omega C_a} + U_a \left(R_a + j\omega M_a + \frac{1}{j\omega C_a} \right) = -p_2 e^{j\omega t} \quad (4)$$

Here, U_D means the volume velocity of the diaphragm, and U_a is the volume velocity through the acoustic resistance. p_1 , p_2 represent the sound pressure entering from the front and back of the transducer, respectively. The net pressure difference can be expressed as (a detailed derivation is given in Note S10):

$$p_D = U_D Z_{ad} = \frac{Z_{ad} \left[R_a p_1 + j \left(\omega M_a p_1 - \frac{p_1 - p_2}{\omega C_a} \right) \right]}{Z_{ad} R_a + \frac{M_a}{C_a} - j \left(\frac{R_a + Z_{ad}}{\omega C_a} - \omega Z_{ad} M_a \right)} e^{j\omega t} \quad (5)$$

2.3. Simulation of multiple physical fields

The whole simulation process is shown in Fig. 1d, which depicts the acoustic pressure field, structural mechanics field, electrostatic field, and circuits in COMSOL. Besides, the acoustic structural mechanics coupling describes the deformation caused by the acoustic vibration, and a moving grid is added for tracking the changes in the physical field. Both frequency domain and transient characteristics are calculated, the former is suited for all frequency-domain simulations with harmonic variations of the pressure field while the latter can be applied to time-dependent simulations with arbitrary time-dependent fields and sources. The structural mechanics part is determined by solving mechanical equations of motion whereby displacements, stresses, and strains are found. Electrostatics is used to compute the electric field, electric displacement field, and potential distributions in dielectrics under conditions where the electric charge distribution is explicitly prescribed. Circuit diagrams allow to model currents and voltages including contributions from voltage and current sources, resistors, capacitors, and inductors. Acoustic waves emitted by the sound source lead to vibration and deformation of the diaphragm. The deformation of the diaphragm under the action of sound pressure and Coulomb force will not only radiate sound waves and influence the distribution of acoustic waves in return but also cause a redistribution of surface charges and generate current in the external circuit load. The combined effects of sound source excitation, sound field distribution, diaphragm deformation, electric field, and external circuit load will affect the output of the transducer.

2.4. Diaphragm vibration behavior analysis

The most important component of the TENG acoustic transducer, the diaphragm, vibrates as a function of the amplitude and frequency of the incoming acoustic field. As a thin circular diaphragm with a fixed edge (Fig. 2a), its vibration mode satisfies the Helmholtz equation as well as the boundary condition [40]:

$$\frac{1}{r} \frac{\partial}{\partial r} \left(r \frac{\partial}{\partial r} \eta \right) + \frac{1}{r^2} \frac{\partial^2}{\partial \theta^2} \eta - \frac{1}{c^2} \frac{\partial^2 \eta}{\partial t^2} = 0, \quad \eta_{(r=a)} = 0 \quad (6)$$

where η is the displacement of the diaphragm, r and a are the polar radius and diaphragm radius respectively, θ represents the polar angle, and c denotes the wave velocity.

In the case of circular symmetry, the displacement of diaphragm vibration η is independent of polar angle θ , $\frac{\partial \eta}{\partial \theta} = 0$ (characterization of performance all base on this circular symmetry case). The solution to Eq. (6) can be expressed as [40]:

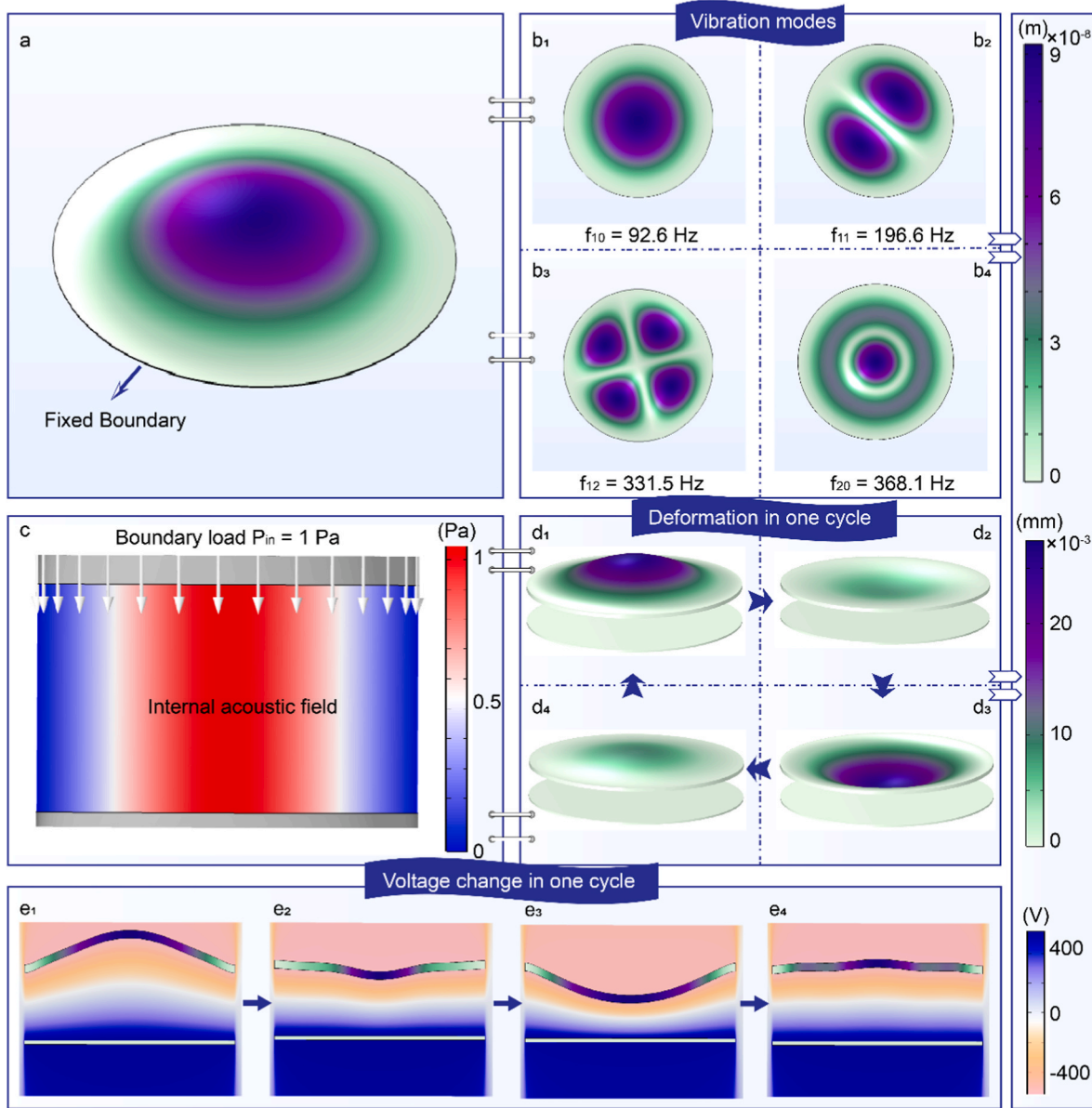


Fig. 2. Vibration modes of the diaphragm as well as its deformation and potential change in one cycle (a) First four order vibration modes of PTFE and Cu diaphragm with fixed boundary: 92.6 Hz, 196.6 Hz, 331.5 Hz, and 368.1 Hz, corresponding to f_{10} (nodal circle number $n = 1$ and nodal diameter number $m = 0$), f_{11}, f_{12} and f_{20} . (b) An internal acoustic field of TENG under the pressure of 1 Pa applied to the diaphragm. (c) Deformation of the diaphragm in one cycle under the pressure of 1 Pa. (d) Potential change of diaphragm due to deformation under the pressure of 1 Pa.

$$\eta_n(t, r) = [A_n J_0(k_n r) + B_n N_0(k_n r)] e^{j\omega t} \quad (7)$$

where $J_0(x)$ and $N_0(x)$ are the zero-order Bessel function and zero-order Neumann functions, respectively. k_n is the wavenumber. A_n and B_n are coefficients determined by the boundary conditions. Notice that the zero-order Neumann function diverges when its argument is zero, i.e., $\lim_{x \rightarrow 0} N_0(x) = \infty$, which is inconsistent with the diaphragm vibration. Thus, $B_n = 0$. By taking the boundary condition in Eq. (6) into account, $J_0(k_n a) = 0$ is obtained. Note that solutions to the zero-order Bessel function are μ_n , which can also be expressed as $k_n a = \mu_n$. Eigenfrequencies for this diaphragm [40]:

$$f_n = \mu_n \frac{c}{2\pi a} = \frac{\mu_n}{2\pi a} \sqrt{\frac{T}{\sigma}} \quad (8)$$

T and σ represent the stretching force and the surface mass density respectively. Eq. (7) can be expressed as [40]:

$$\eta_n(t, r) = A_n J_0\left(\frac{\mu_n}{a} r\right) e^{j\omega t} \quad (9)$$

For asymmetric cases, the solution becomes [40]:

$$\eta_{nm}(t, r, \theta) = A_{nm} J_m\left(\frac{\mu_{nm}}{a} r\right) \cos(m\theta - \varphi_m) e^{j\omega t} \quad (10)$$

$J_m(x)$, instead of $J_0(x)$, represents the m -order Bessel function and θ is the polar angle. μ_n is replaced by μ_{mn} to satisfy the boundary condition $J_m(k_{mn} a) = 0$. The first four eigenmodes are shown in Fig. 2b₁ to Fig. 2b₄. m is the nodal diameter number. $m = 0$ represents symmetric vibrations (Fig. 2b₁, Fig. 2b₄) and $m > 0$ corresponds to asymmetric vibrations (Fig. 2b₂, Fig. 2b₃). n is the nodal circle number and corresponds to the number of nodes in the radial direction. If an external pressure is applied to the diaphragm (Fig. 2c), the diaphragm forced vibration becomes [40]:

$$\eta_{nm}(t, r) = \frac{p_{in}}{k^2 T} \left[\frac{J_m(\frac{\mu_{nm}}{a} r)}{J_m(\mu_{nm})} - 1 \right] e^{j\omega t} \quad (11)$$

where p_{in} is the boundary load applied to the diaphragm. A detailed derivation can be found in Note S3. Under external load excitations, the deformation and voltage in one cycle are displayed in Fig. 2d and e, respectively.

2.5. Fundamental performance of TENG acoustic transducer

As shown in Fig. 3a, the characterization of the TENG acoustic transducer output performance is based on a symmetric excitation. By imposing an external pressure load at different frequencies, electric and mechanic properties will change accordingly.

For the conductor-dielectric contact-mode TENG, the output voltage can be expressed as [41]:

$$V = -\frac{Q}{Se_0} \left(\frac{d}{\varepsilon_r} + x(t, r, \theta) \right) + \frac{\sigma x(t, r, \theta)}{\varepsilon_0} \quad (12)$$

A more detailed derivation is given in Note S4. In Eq. (12), V is the potential difference between the two electrodes, and Q is defined as the amount of charge transferred. ε_0 , ε_r represent the vacuum permittivity

and the relative permittivity of the dielectric (PTFE), respectively. S is the contact separation area, and σ represents the surface charge density. Since the vibration displacement of the diaphragm is related to its position, the contact separation distance x can be written as:

$$x(t, r, \theta) = h + \eta(t, r, \theta) \quad (13)$$

h is the initial distance between the electrode and the dielectric, η is the vibration displacement of the diaphragm, which is marked in Fig. 3b. The vibration displacement η is highly dependent on the frequency, which is illustrated in Fig. 2b. Fig. 3c shows the diaphragm's deformation by choosing six examples of typical frequency excitations. It is important to determine how the diaphragm vibrates under the influence of electrostatic forces. Fig. S4 compares the displacement of the diaphragm under the action of electrostatic forces with the maximum displacement of the diaphragm due to a pressure load. Since the former is significantly smaller than the latter, it is reasonable to discard the effects of electrostatic forces on the diaphragm displacement. We also notice that TENG acoustic transducer performs better at low frequencies compared to high frequencies which can be explained by Eq. (11). According to Eq. (11), The displacement of the diaphragm is inversely proportional to the quadratic power of the wave number k (the wave number k and frequency f can be converted by equation $k = \frac{2\pi f}{c}$), which means that for forced vibrations, the higher the frequency, the smaller

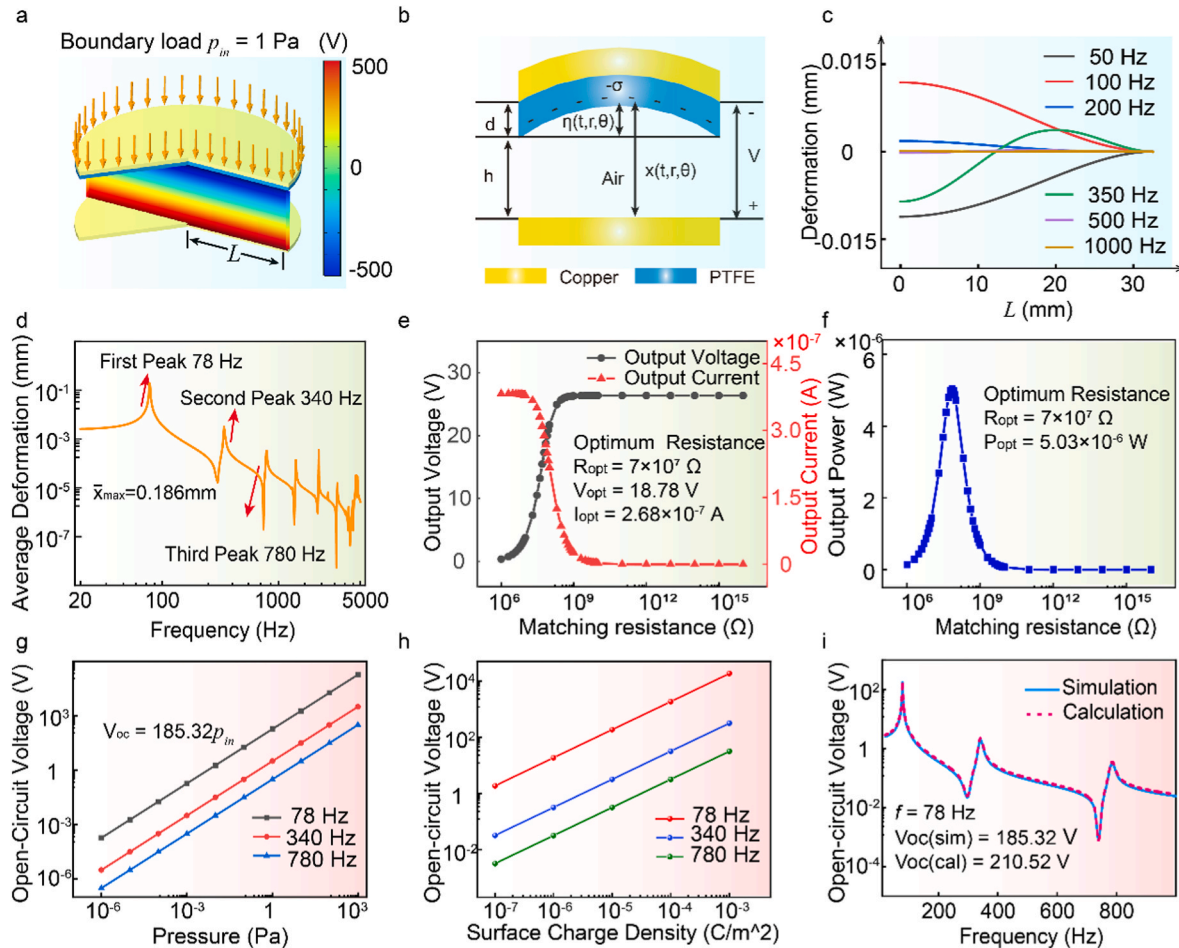


Fig. 3. Diaphragm deformation and electrical output under pressure load. (a) TENG initial potential under a pressure load of 1 Pa. (b) Theoretical model diagram of TENG acoustic transducer (conductor-to-dielectric contact-mode TENG). (c) Diaphragm deformation at 50, 100, 200, 350, 500, and 1000 Hz. (d) Average deformation of the diaphragm within 20–5000 Hz (First three peaks appear at 78 Hz, 340 Hz, and 780 Hz). (e) Dependence of output voltage and output current on external matching resistance. (f) Dependence of output power on external matching resistance. (g) Dependence of open-circuit voltage on sound pressure p_{in} . (h) Open-circuit voltage output for different surface charge densities at the resonant frequency. (i) Comparison of simulated and calculated open-circuit voltage of TENG acoustic transducer within 20–1000 Hz. At 78 Hz, the simulated open-circuit voltage is 185.32 V while the calculated open-circuit voltage is 210.52 V.

the displacement of the diaphragm and Fig. 3d verifies this. To obtain a stable response in a wider frequency band, a possible way is to change the size of the TENG. Fig. S5 discusses the effect of different sizes and thicknesses of the diaphragm on the bandwidth. As the diaphragm's diameter and thickness increase, the bandwidth increases but the sensitivity decreases. Because of the diverse distribution of the diaphragm's vibration, an average deformation $\bar{\eta}$ is proposed to describe the amplitude of vibration. $\bar{x} = h + \bar{\eta}$ and Eq. (12) can be written as:

$$V(t) = -\frac{Q}{S\epsilon_0} \left(\frac{d}{\epsilon_r} + \bar{x}(t) \right) + \frac{\sigma \bar{x}(t)}{\epsilon_0} \quad (14)$$

The diaphragm will have bigger deformation around its eigenfrequency in agreement with the first three peaks in Fig. 3c (78 Hz, 340 Hz, and 780 Hz) which are smaller compared to the eigenfrequencies calculated in Fig. 2b. A possible reason is a self-radiation impedance (Note S3). Mass resistance further decreases the resonance frequency. By giving a simple harmonic excitation, the open-circuit voltage behaves like a sinusoidal wave. The output voltage for different resistors can be found in Fig. S6. The resistor, utilized as external loads, also has a significant influence on the output. The TENG acoustic transducer can be regarded as a voltage source with variable resistance. The higher the external resistance is, the higher is the voltage and the current decreases. When the external resistance approaches the internal resistance of the TENG, the peak output power is obtained corresponding to the optimum resistance [28]. As displayed in Fig. 3e, the voltage on the resistor increases with increasing load resistance, while the current shows a reverse trend. As a result, the peak output power reaches its maximum value (5.03×10^{-6} W) at an optimum resistance of $70 \text{ M}\Omega$ (Fig. 3f), corresponding to the optimum voltage of 18.78 V and optimum current of 2.68×10^{-7} A. Considering the model's size, the TENG acoustic transducer is capable of delivering a power density of 152 mW/m^2 and 843 W/m^3 under a sound pressure of 1 Pa, which is consistent with the TENG output made in Ref. 30. In addition to frequency, the average separation distance \bar{x} is closely related to sound pressure. Keeping 78 Hz as input excitation frequency, change sound pressure and we can obtain a linear approximation relation between output voltage V and input pressure p_{in} : $V = 185.32 p_{in}$, which means a sound pressure of 1 Pa can produce a voltage output of 185.32 V (Fig. 3g). When the resistance R is very large, the circuit can be approximately considered to be in an open-circuit state, where the transferred charge Q is approximately zero, and the potential V can be written as:

$$V(t) = \frac{\sigma \bar{x}(t)}{\epsilon_0} = \frac{\sigma h}{\epsilon_0} + \frac{\sigma}{\epsilon_0} \bar{\eta}(t) \quad (15)$$

In Eq. (15), the first term $\frac{\sigma h}{\epsilon_0}$, denoted as $V_{initial}$, does not vary with contact separation distance in vibration. The second term is the open-circuit voltage during stable vibration, denoted as V_{oc} :

$$V_{oc}(t) = \frac{\sigma}{\epsilon_0} \bar{\eta}(t) \quad (16)$$

According to Eq. (16), besides the average deformation $\bar{\eta}$, the surface charge density σ is another important factor affecting V_{oc} . Fig. 3h shows the open-circuit voltage at the characteristic frequency, which is linearly and positively related to the surface charge density, consistent with Eq. (16). In addition, we also confirmed the correctness of this model by comparing the calculation and simulation results of Eq. (16). At the resonant frequency of 78 Hz, the simulated open-circuit voltage is 185.32 V while the calculated open-circuit voltage is 210.52 V.

2.6. Influence of acoustic field and working environment

The simulations above are finished in an ideal air domain using pressure load as the excitation input. In practical situations, due to a series of factors such as imperfect sound source, acoustic wave propagation, and impedance matching, the performance is often worse than

the ideal situation. Acoustic waves emitted by the sound source can be divided into three types: plane waves, cylindrical waves, and spherical waves [40]. In the one-dimensional sound field or tubular sound field, sound waves usually propagate as plane waves while in three-dimensional space, the point sound source induces spherical waves. Fig. 4a shows the acoustic field distribution for an incident plane wave with a pressure of 1 Pa and 100 Hz, and Fig. 4c shows the diaphragm displacement and the distribution of the electric field. Similarly, Fig. 4b shows the spatial distribution of the sound field generated by the vibration of the point sound source with 10^8 W/m^3 source intensity at 100 Hz, and Fig. 4d shows the vibration velocity of the point source and the spatial electric field distribution. Comparing the frequency responses of plane wave and spherical wave sound fields, it is noticeable that the TENG acoustic transducer has a better response at lower frequencies for a plane wave acoustic field, while the response for a spherical wave acoustic field is better at high frequencies (Fig. 4e). The main reason is the form of the sound source excitation. More specifically, the plane wave excitation uses the background sound field, and the sound pressure does not change with the change of frequency corresponding to the sound field environment under ideal conditions. For the spherical wave excited by a point sound source, the sound field excited under constant power increases with the increase of frequency. (a detailed derivation and explanation can be found in Note S8). Besides, independent of the acoustic field environment, the transducer reaches the maximum output near its resonance frequency (the first three resonance frequencies appear at 78 Hz, 340 Hz, and 780 Hz respectively, consistent with pressure load excitation).

Another factor that requires attention is the sound field environment. For typical experimental conditions, the acoustic performance is measured in an anechoic chamber which is used to minimize the internal sound reflection and external noise. For realistic environments, the reverberation chamber is a better choice to describe the rigid-wall space formed by the wall, floor, and ceiling. A reverberation chamber is designed to describe a diffuse or random incident acoustic field (or a chamber with uniform sound energy distribution and random sound incident direction in a short time). Different from the anechoic chamber, the change in impedance these hard exposed surfaces present to the incident sound is so large that virtually all of the acoustic energy that hits a surface is reflected into the room. In this simulation, we use a hard acoustic field boundary to simulate the reverberation chamber (Fig. S8) and the perfect matching layer, which absorbs the acoustic waves, to simulate the experimental environment of the anechoic chamber (Fig. 4a and b). In the simulated sound field, the sound pressure p can be regarded as two parts - the direct sound p_D and the reverberation sound p_R . The direct sound and the reverberation sound are incoherent, so the superposition in space is the addition of energy density, which is given by Ref. [38]:

$$p^2 = p_D^2 + p_R^2 \quad (17)$$

which can be written as [40]:

$$p = \sqrt{2S_0 V_0 \rho_0 c_0 \left(\frac{1}{4\pi r^2} + \frac{4}{R} \right)} \quad (18)$$

where, S_0 , V_0 describe the power density and volume of the radiation sphere source. ρ_0 , c_0 represent the density and sound speed of air. r is the distance to the sound source and R is room constant, which is related to surface area S and sound absorption coefficient α by $R = \frac{Sa}{1-\alpha}$ (a detailed derivation and explanation are given in Note S9). According to Eq. (18), an acoustic matching layer means large absorption coefficient α and room constant R , which will significantly reduce the reverberation sound p_R . Reverberation sound is evenly distributed in space and therefore weakens the response of the direct sound. However, using an acoustic matching layer, the reverberation sound is absorbed, and the diaphragm is mainly affected by the direct sound. As a result, using an

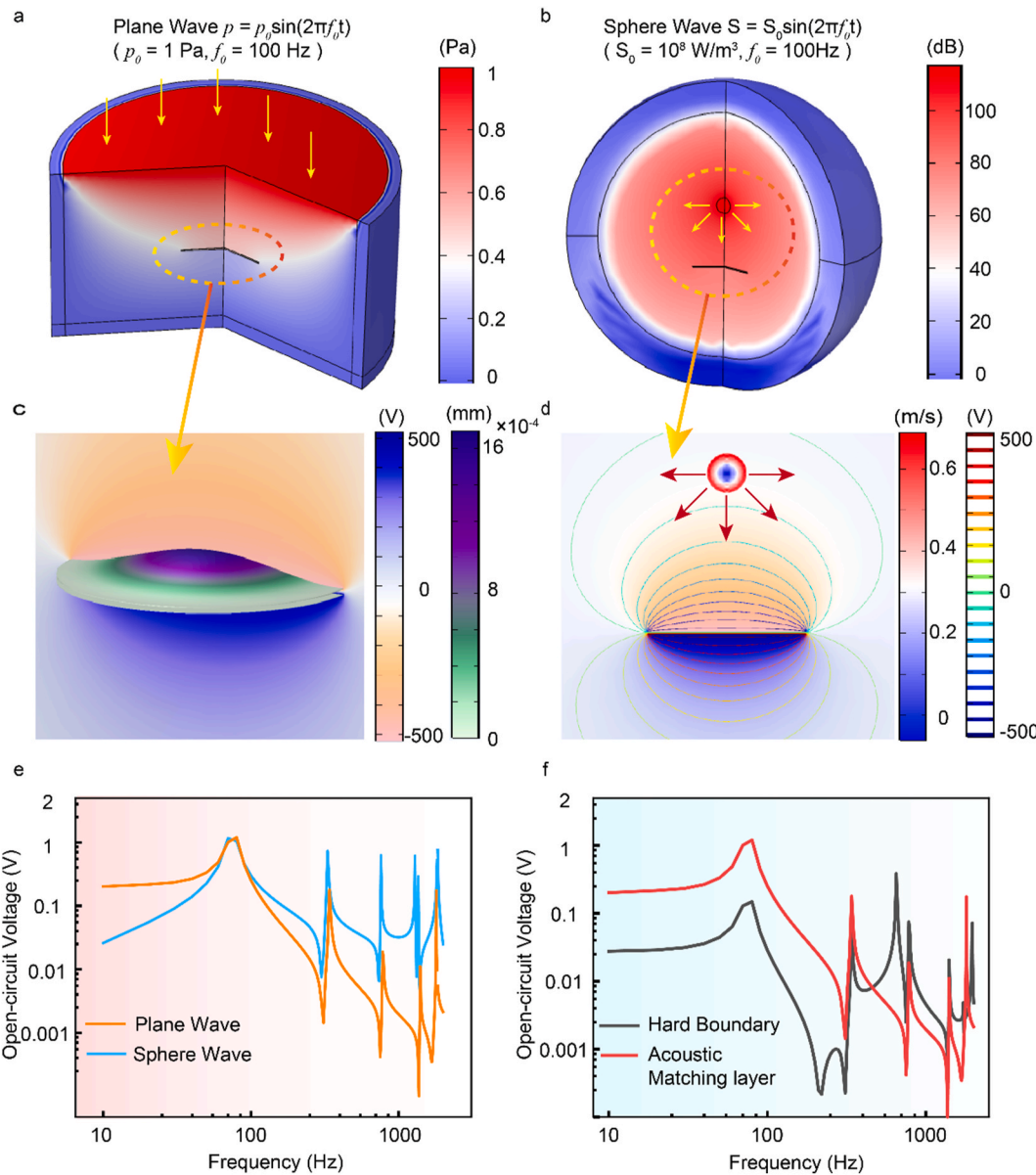


Fig. 4. Performance of TENG acoustic transducer in the acoustic field (a) Acoustic field distribution in space under the excitation of the plane sound wave of 1 Pa (with a matching layer outside to absorb sound wave and simulate the environment of the total anechoic chamber). (b) Acoustic field distribution in space excited by 10^8 W/m^3 point source (with a matching layer outside to absorb sound wave). (c) Diaphragm vibration and potential distribution of TENG acoustic transducer. (d) Vibration velocity and spatial potential distribution of the point source acoustic field distribution excited by 10^8 W/m^3 point source (with a matching layer outside to absorb sound wave). (e) Open circuit voltage within 20–2000 Hz under the plane acoustic wave and spherical wave excitation. (f) Effect of matching layer on output open circuit voltage excited by a plane wave.

acoustic matching layer, the response of the diaphragm to vibration is more sensitive. Returning to the simulation results: For the plane wave acoustic field, a significant increase is found in the low-frequency band (about 17 dB) in the anechoic chamber environment compared to the reverberation environment, but no significant increase in the high-frequency band is obtained (Fig. 4f). In addition, there is no obvious difference between the spherical wave acoustic field when comparing anechoic and reverberation chambers (Fig. S9).

2.7. Opening holes on TENG acoustic transducer

The opening holes are helpful to improve the performance of the TENG acoustic transducers. According to the different working principles, acoustic transducers can be divided into pressure type (Fig. 5a₁), pressure-gradient type (Fig. 5a₂) and a combination of pressure and

pressure-gradient type (Fig. 5a₃) (see Note S10 for the working principle of the three different types microphones). A TENG acoustic transducer with holes on the back can be regarded as the last type. On the one hand, the opening holes can change the air circulation to improve the sensitivity of the transducer. On the other hand, it will also reduce the effective contact area which results in reduction of the surface charge and the output of the transducer. Eq. (5) can be transformed to get:

$$p_D = \frac{Z_{ad} \left[R_a p_1 \omega + j \left(\omega^2 M_a p_1 - \frac{p_1 - p_2}{C_a} \right) \right]}{\left(Z_{ad} R_a + \frac{M_a}{C_a} \right) \omega - j \left(\frac{R_a + Z_{ad}}{C_a} - \omega^2 Z_{ad} M_a \right)} e^{j\omega t} \quad (19)$$

Here, the acoustic mass $M_a = \frac{\rho_0 l_0}{S_0}$, describes the equivalent mass of the air column vibration within the opening holes. $C_a = \frac{V_0}{\gamma P_0}$, represents the elastic effect of the cavity in the vibration. R_a is the resistance of the

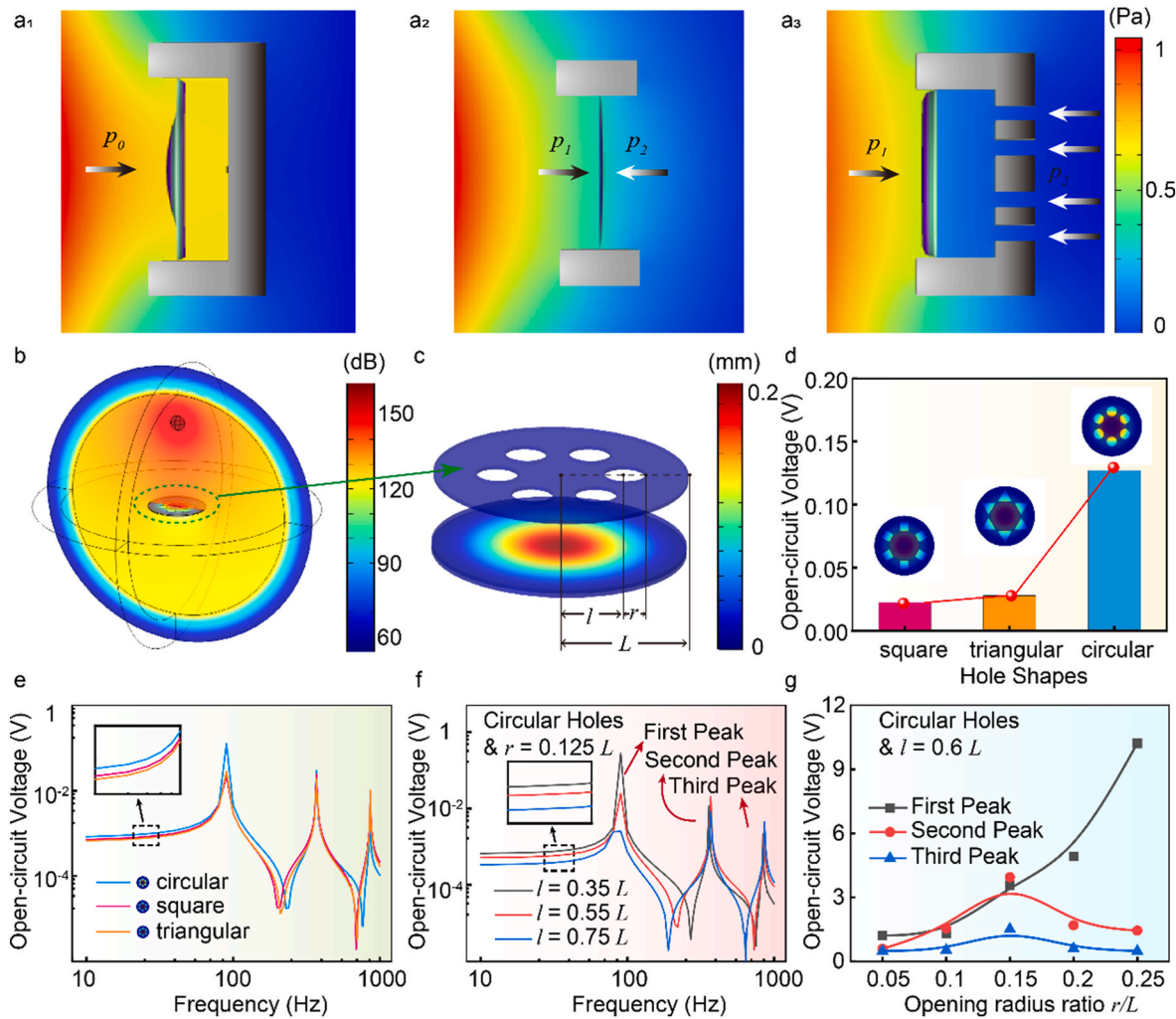


Fig. 5. Effect of opening holes on TENG acoustic transducer (a) Schematic diagram of pressure acoustic transducer (a₁), pressure-gradient acoustic transducer (a₂), and a combination of pressure and pressure-gradient acoustic transducer (a₃). (b) TENG acoustic transducer in acoustic field excited by a point source. (c) Structure diagram of TENG acoustic transducer. (d) Effect of opening shape (circular, square and triangular holes) on open-circuit voltage. (e, f) Effect of opening shape and position ($r = 0.125 L$, $l = 0.35 L$, $0.55 L$ and $0.75 L$, L represents the radius of TENG device.) on open-circuit voltage within 20–1000 Hz. (g) Effect of opening size ($l = 0.6 L$, $r = 0.05 L$, $0.10 L$, $0.15 L$, $0.20 L$ and $0.25 L$) on open-circuit voltage of first three peaks.

sound flow through the holes. ρ_0 , l_0 , S_0 mean air density, hole depth, and opening area, respectively. V_0 , P_0 , γ represent the cavity volume, atmospheric pressure, and specific heat ratio, respectively. At low frequencies, the net pressure difference is $p_D \approx \frac{Z_{ad}(p_1-p_2)}{R_a+Z_{ad}}$. Reducing the acoustic resistance R_a can effectively improve the pressure on the membrane and improve its output. While at high frequencies, $p_D \approx \frac{Z_{ad}p_1}{Z_{ad}+r} = p_1$, acoustic resistance has little effect on p_D . The TENG acoustic transducer is placed in the acoustic field generated by the spherical source excitation (Fig. 5b), and a matching layer is used to absorb the diffused acoustic waves to simulate the anechoic chamber environment. The transducer structure is shown in Fig. 5c (inverted) with r as the opening radius and L as the distance between the hole center and the transducer. The narrow space of the opening will change the acoustic structure and affect the calculation of the acoustic field. Note S11 discusses this case, demonstrating that pressure acoustic modeling is still a viable approach. Compared with the TENG acoustic transducer without apertures, in the case of $l = 0.60 L$ and $r = 0.05 L$, the output of a TENG with circular holes in the frequency band of 20–1000 Hz is improved by an average of 5.31 times (Fig. S15). Before exploring the influence of opening size and position, we first studied the influence of opening shape on output, because the ability of the sound flow to pass through the holes is closely related to the holes' shape. As shown in Fig. 5d, under

the same opening area and position, the circular openings has the greatest improvement on the output, especially in the low-frequency band (Fig. 5e). At the resonant frequency of 78 Hz, the output of circular apertures is improved by about 5 times and 4 times compared to square and triangular apertures, respectively. Compared to square and triangular openings, the acoustic resistance is minimal under the circular openings, so the sound flow can pass through the hole easily, especially in the low-frequency band. The position of the openings also greatly affects the passage of sound flow. Since the periphery of the diaphragm is fixed, the area with large displacement is often concentrated in the center of the diaphragm, especially for axisymmetric vibration modes. Therefore, the openings near the center of the diaphragm can result in effective output improvement. Under the condition of circular openings and unchanged opening size, the closer the opening position is to the center, the greater output will be obtained, which confirms the theoretical analysis (Fig. 5f). In the frequency range 20–1000 Hz, the output of the nearest opening position ($l = 0.35 L$) is increased by an average of 3 times compared with a higher opening position ($l = 0.75 L$). The first three peaks, also consistent with calculations before, appear at 78 Hz, 340 Hz, and 780 Hz. The effect of opening size is the most intuitive. In the lower frequency range, the higher-order term of ω can be ignored, so Eq. (19) can be transformed

into:

$$p_D = \frac{Z_{ad} \left[R_a p_1 \omega - j \left(\frac{p_1 - p_2}{C_a} \right) \right]}{\left(Z_{ad} R_a + \frac{M_a}{C_a} \right) \omega - j \left(\frac{R_a + Z_{ad}}{C_a} \right)} e^{j\omega t} \quad (20)$$

From Eq. (20), it follows that reducing acoustic mass M_a increases p_D . Larger opening holes ($S_D = \pi r^2$) mean smaller acoustic mass M_a and increased sound pressure difference p_D , but reducing the surface charge density of the contact. The influence of the opening size on the output is shown in Fig. 5g (a detailed frequency response can be found in Fig. S16). For circular openings and an opening distance of $0.6L$, the increase of the opening size in the low-frequency effectively improves the output but it has little effect on the output in the high-frequency band. In addition, the induced charge decreases due to the increase of the opening size which also leads to the reduction of output. Fig. S17 further demonstrates that the open-circuit voltage will ultimately drop if the openings' size continue to increase. As a result, the positive effect of the openings on the sound flow at low frequencies is larger than the negative effect brought by the reduction of the induced charge, while at high frequencies, the effect of the openings is weakened, and the negative effect of the reduction of the charge seems to be prominent. In the whole frequency range of 20–1000 Hz, the average output when $r = 0.25 L$ is 3.7 times that when $r = 0.05 L$. In Fig. S18, the number of openings as a factor that affects the output is also investigated. The number of openings' impact the output, however, the effect is not significant when the opening ratio and the opening location remain constant. In summary, circular openings, a closer position, and a larger opening size can effectively improve the output of the TENG acoustic transducer at low frequencies, while the influence of induced charge should be considered at high frequencies.

3. Conclusion

Coupling the acoustic, structural mechanics, and electrostatic fields, a theoretical model of a TENG for acoustic energy conversion is proposed, which provides optimal strategies for improving the output performance of the TENG acoustic transducer. Through finite element method simulations, we discuss the acoustic, mechanical, and electrical factors affecting the performance of the TENG acoustic transducer. It is demonstrated that the transducer output is linearly and positively correlated with the diaphragm displacement, and reaches maximum output near the diaphragm resonance frequency. Besides, the sound field also plays an important role in the testing of TENG. Under reverberation room conditions, the output of the TENG acoustic transducer is significantly reduced, by 17 dB, for plane wave excitation. On this basis, openings, as an effective method to improve the average membrane displacement of the diaphragm, are put forward and analyzed to improve the electrical output of the TENG acoustic transducer. Larger opening sizes and closer opening positions to the center of the TENG are of great help to improve the output. The present theoretical framework establishes a self-contained theory of TENGs and electroacoustic energy conversion through multiple physical field couplings and provides a new perspective for TENG theoretical research in the direction of thermo-electric conversion, electromechanical conversion, and so on.

Credit author statement

Zhiwei Zhang: Conceptualization, Software, Formal analysis, Investigation, Data Curation, Writing - Original Draft **Jiajia Shao:** Conceptualization, Methodology, Validation, Writing - Review & Editing **Yang Nan:** Writing - Review & Editing **Morten Willatzen:** Conceptualization, Methodology, Writing - Review & Editing, Supervision **Zhong Lin Wang:** Writing - Review & Editing, Supervision.

Data and materials availability

All data needed to evaluate the conclusions in the paper are present in the paper and/or the Supplementary Materials. Additional data related to this paper may be requested from the authors.

Declaration of competing interest

The authors declare that they have no known competing financial interests or personal relationships that could have appeared to influence the work reported in this paper.

Acknowledgments

Funding: Research Z.W. Zhang and J.J. Shao contributed equally to this work. Research supported by the National Natural Science Foundation of China (Grant Nos. 62001031, 51702018, and 51432005), National Key R & D Project from Minister of Science and Technology (Grant No. 2016YFA0202704), Fundamental Research Funds for the Central Universities (Grant No. E0E48957).

Appendix A. Method

The FEM simulation in multiple physical fields is carried out using the COMSOL software. The characteristic frequency analysis in structural mechanics is used to calculate the vibration mode of the boundary fixed diaphragm. Acoustic pressure fields (in frequency domain) lead to the generation and propagation of sound waves (using linear sound source to generate the plane wave, and point sound source to generate spherical wave). The electrostatic field is proposed to describe the change of potential caused by the diaphragm vibration while the circuit connects the two electrodes of the device. The acoustic field and structural mechanics are coupled by acoustic-structure interaction, and the displacement and deformation of the model are optimized by moving grids. For each model, the response in the frequency domain and time domain are calculated to investigate how frequency, sound pressure, external load, openings, and other field quantities affect electric output. Details and the parameters utilized in computations can be found in the Supplementary Materials.

Appendix B. Supplementary data

Supplementary data to this article can be found online at <https://doi.org/10.1016/j.mtphys.2022.100784>.

References

- [1] Z.L. Wang, On Maxwell's displacement current for energy and sensors: the origin of nanogenerators, Mater. Today 20 (2017) 74–82, <https://doi.org/10.1016/j.mattod.2016.12.001>.
- [2] F. Xi, Y. Pang, W. Li, T. Jiang, L. Zhang, T. Guo, G. Liu, C. Zhang, Z.L. Wang, Universal power management strategy for triboelectric nanogenerator, Nano Energy 37 (2017) 168–176, <https://doi.org/10.1016/j.nanoen.2017.05.027>.
- [3] C. Wu, A.C. Wang, W. Ding, H. Guo, Z.L. Wang, Triboelectric nanogenerator: a foundation of the energy for the new era, Adv. Energy Mater. 9 (2019) 1802906, <https://doi.org/10.1002/aenm.201802906>.
- [4] G.R. Chen, Y.Z. Li, M. Bick, J. Chen, Smart textiles for electricity generation, Chem. Rev. 120 (2020) 3668–3720, <https://doi.org/10.1021/acs.chemrev.9b00821>.
- [5] Z.L. Wang, From contact electrification to triboelectric nanogenerators, Rep. Prog. Phys. 84 (2021) 096502, <https://doi.org/0000-0002-5530-0380>.
- [6] X. Zhao, H. Askari, J. Chen, Nanogenerators for smart cities in the era of 5G and Internet of Things, Joule 5 (2021) 1391–1431, <https://doi.org/10.1016/j.joule.2021.03.013>.
- [7] W. Li, D. Torres, R. Díaz, Z. Wang, C. Wu, C. Wang, Z. Lin Wang, N. Sepúlveda, Nanogenerator-based dual-functional and self-powered thin patch loudspeaker or microphone for flexible electronics, Nat. Commun. 8 (2017) 15310, <https://doi.org/10.1038/ncomms15310>.
- [8] J. Chen, Z.L. Wang, Reviving vibration energy harvesting and self-powered sensing by a triboelectric nanogenerator, Joule 1 (2017) 480–521, <https://doi.org/10.1016/j.joule.2017.09.004>.

- [9] X. Wang, J. Song, J. Liu, Z.L. Wang, Direct-current nanogenerator driven by ultrasonic waves, *Science* 316 (2007) 102–105, <https://doi.org/10.1126/science.1139366>.
- [10] X. Wang, J. Liu, J. Song, Z.L. Wang, Integrated nanogenerators in biofluid, *Nano Lett.* 7 (2007) 2475–2479, <https://doi.org/10.1021/nl0712567>.
- [11] A. Li, Y. Zi, H. Guo, Z.L. Wang, F.M. Fernández, Triboelectric nanogenerators for sensitive nano-coulomb molecular mass spectrometry, *Nat. Nanotechnol.* 12 (2017) 481–487, <https://doi.org/10.1038/nano.2017.17>.
- [12] R. Hinchet, H.J. Yoon, H. Ryu, M.K. Kim, E.K. Choi, D.S. Kim, S.W. Kim, Transcutaneous ultrasound energy harvesting using capacitive triboelectric technology, *Science* 365 (2019) 491–494, <https://doi.org/10.1126/science.aan3997>.
- [13] J. Shao, M. Willatzen, Y. Shi, Z.L. Wang, 3D mathematical model of contact-separation and single-electrode mode triboelectric nanogenerators, *Nano Energy* 60 (2019) 630–640, <https://doi.org/10.1016/j.nanoen.2019.03.072>.
- [14] Z.L. Wang, A.C. Wang, On the origin of contact-electrification, *Mater. Today* 30 (2019) 34–51, <https://doi.org/10.1016/j.mattod.2019.05.016>.
- [15] Z.L. Wang, On the first principle theory of nanogenerators from Maxwell's equations, *Nano Energy* 68 (2020) 104272, <https://doi.org/10.1016/j.nanoen.2019.104272>.
- [16] Z.L. Wang, Triboelectric nanogenerators as new energy technology and self-powered sensors – principles, problems and perspectives, *Faraday Discuss* 176 (2014) 447–458, <https://doi.org/10.1039/C4FD00159A>.
- [17] J. Wang, S. Li, F. Yi, Y. Zi, J. Lin, X. Wang, Y. Xu, Z.L. Wang, Sustainably powering wearable electronics solely by biomechanical energy, *Nat. Commun.* 7 (2016) 12744, <https://doi.org/10.1038/ncomms12744>.
- [18] Z. Wen, M.-H. Yeh, H. Guo, J. Wang, Y. Zi, W. Xu, J. Deng, L. Zhu, X. Wang, C. Hu, L. Zhu, X. Sun, Z.L. Wang, Self-powered textile for wearable electronics by hybridizing fiber-shaped nanogenerators, solar cells, and supercapacitors, *Sci. Adv.* 2 (2016) 1600097, <https://doi.org/10.1126/sciadv.1600097>.
- [19] X. He, Y. Zi, H. Yu, S.L. Zhang, J. Wang, W. Ding, H. Zou, W. Zhang, C. Lu, Z. L. Wang, An ultrathin paper-based self-powered system for portable electronics and wireless human-machine interaction, *Nano Energy* 39 (2017) 328–336, <https://doi.org/10.1016/j.nanoen.2017.06.046>.
- [20] J. Cheng, W. Ding, Y. Zi, Y. Lu, L. Ji, F. Liu, C. Wu, Z.L. Wang, Triboelectric microplasma powered by mechanical stimuli, *Nat. Commun.* 9 (2018) 3733, <https://doi.org/10.1038/s41467-018-06198-x>.
- [21] G. Cheng, H. Zheng, F. Yang, L. Zhao, M. Zheng, J. Yang, H. Qin, Z. Du, Z.L. Wang, Managing and maximizing the output power of a triboelectric nanogenerator by controlled tip-electrode air-discharging and application for UV sensing, *Nano Energy* 44 (2018) 208–216, <https://doi.org/10.1016/j.nanoen.2017.11.062>.
- [22] X.S. Zhang, M.D. Han, R.X. Wang, F.Y. Zhu, Z.H. Li, W. Wang, H.X. Zhang, Frequency-multiplication high-output triboelectric nanogenerator for sustainably powering biomedical microsystems, *Nano Lett.* 13 (2013) 1168–1172, <https://doi.org/10.1021/nl3045684>.
- [23] J. Yang, J. Chen, Y. Su, Q. Jing, Z. Li, F. Yi, X. Wen, Z. Wang, Z.L. Wang, Eardrum-inspired active sensors for self-powered cardiovascular system characterization and throat-attached anti-interference voice recognition, *Adv. Mater.* 27 (2015) 1316–1326, <https://doi.org/10.1002/adma.201404794>.
- [24] J. Chen, G. Zhu, J. Yang, Q. Jing, P. Bai, W. Yang, X. Qi, Y. Su, Z.L. Wang, Personalized keystroke dynamics for self-powered human-machine interfacing, *ACS Nano* 9 (2015) 105–116, <https://doi.org/10.1021/nn506832w>.
- [25] Z. Zhao, L. Zhou, S. Li, D. Liu, Y. Li, Y. Gao, Y. Liu, Y. Dai, J. Wang, Z.L. Wang, Selection rules of triboelectric materials for direct-current triboelectric nanogenerator, *Nat. Commun.* 12 (2021) 4686, <https://doi.org/10.1038/s41467-021-25046-z>.
- [26] Z. Ren, Z. Wang, F. Wang, S. Li, Z.L. Wang, Vibration behavior and excitation mechanism of ultra-stretchable triboelectric nanogenerator for wind energy harvesting, *Extreme Mech. Lett.* 45 (2021) 101285, <https://doi.org/10.1016/j.eml.2021.101285>.
- [27] J. Yang, J. Chen, Y. Liu, W. Yang, Y. Su, Z.L. Wang, Triboelectrification-based organic film nanogenerator for acoustic energy harvesting and self-powered active acoustic sensing, *ACS Nano* 8 (2014) 2649–2657, <https://doi.org/10.1021/nn4063616>.
- [28] J. Shao, M. Willatzen, Z.L. Wang, Theoretical modeling of triboelectric nanogenerators (TENGs), *J. Appl. Phys.* 128 (2020) 111101, <https://doi.org/10.1063/5.0020961>.
- [29] J. Shao, D. Liu, M. Willatzen, Z.L. Wang, Three-dimensional modeling of alternating current triboelectric nanogenerator in the linear sliding mode, *Appl. Phys. Rev.* 7 (2020) 011405, <https://doi.org/10.1063/1.5133023>.
- [30] X. Fan, J. Chen, J. Yang, P. Bai, Z. Li, Z.L. Wang, Ultrathin, Rollable, paper-based triboelectric nanogenerator for acoustic energy harvesting and self-powered sound recording, *ACS Nano* 9 (2015) 4236–4243, <https://doi.org/10.1021/acsnano.5b00618>.
- [31] H. Zhao, X. Xiao, P. Xu, T. Zhao, L. Song, X. Pan, J. Mi, M. Xu, Z.L. Wang, Dual-tube helmholtz resonator-based triboelectric nanogenerator for highly efficient harvesting of acoustic energy, *Adv. Energy Mater.* 9 (2019) 1902824, <https://doi.org/10.1002/aem.201902824>.
- [32] M. Yuan, C. Li, H. Liu, Q. Xu, Y. Xie, A 3D-printed acoustic triboelectric nanogenerator for quarter-wavelength acoustic energy harvesting and self-powered edge sensing, *Nano Energy* 85 (2021) 105962, <https://doi.org/10.1016/j.nanoen.2021.105962>.
- [33] J. Shao, Y. Yang, O. Yang, J. Wang, M. Willatzen, Z.L. Wang, Designing rules and optimization of triboelectric nanogenerator arrays, *Adv. Energy Mater.* 11 (2021) 2100065, <https://doi.org/10.1002/aem.202100065>.
- [34] N. Cui, L. Gu, J. Liu, S. Bai, J. Qiu, J. Fu, X. Kou, H. Liu, Y. Qin, Z.L. Wang, High performance sound driven triboelectric nanogenerator for harvesting noise energy, *Nano Energy* 15 (2015) 321–328, <https://doi.org/10.1016/j.nanoen.2015.04.008>.
- [35] F. Chen, Y. Wu, Z. Ding, X. Xia, S. Li, H. Zheng, C. Diao, G. Yue, Y. Zi, A novel triboelectric nanogenerator based on electrospun polyvinylidene fluoride nanofibers for effective acoustic energy harvesting and self-powered multifunctional sensing, *Nano Energy* 56 (2019) 241–251, <https://doi.org/10.1016/j.nanoen.2018.11.041>.
- [36] W. Qiu, Y. Feng, N. Luo, S. Chen, D. Wang, Sandwich-like sound-driven triboelectric nanogenerator for energy harvesting and electrochromic based on Cu foam, *Nano Energy* 70 (2020) 104543, <https://doi.org/10.1016/j.nanoen.2020.104543>.
- [37] N. Arora, S.L. Zhang, F. Shahmiri, D. Osorio, Y.C. Wang, M. Gupta, Z. Wang, T. Starner, Z.L. Wang, G.D. Abowd, SATURN: a thin and flexible self-powered microphone leveraging triboelectric nanogenerator, *Proc. ACM Interact. Mob. Wearable Ubiquitous Technol.* 2 (2018) 1–28, <https://doi.org/10.1145/3214263>.
- [38] H. Guo, X. Pu, J. Chen, Y. Meng, M.H. Yeh, G. Liu, Q. Tang, B. Chen, D. Liu, S. Qi, C. Wu, C. Hu, J. Wang, Z.L. Wang, A highly sensitive, self-powered triboelectric auditory sensor for social robotics and hearing aids, *Sci. Robot.* 3 (2018), <https://doi.org/10.1126/scirobotics.aat2516> eaat2516.
- [39] L.L. Beranek, T.J. Mellow, *Acoustics: Sound Fields and Transducers*, Academic Press, New York, 2012.
- [40] P.M. Morse, K.U. Ingard, *Theoretical Acoustics*, Princeton University Press, Princeton, 1968.
- [41] S. Niu, S. Wang, L. Lin, Y. Liu, Y.S. Zhou, Y. Hu, Z.L. Wang, Theoretical study of contact-mode triboelectric nanogenerators as an effective power source, *Energy Environ. Sci.* 6 (2013) 3576–3583, <https://doi.org/10.1039/C3EE42571A>.